

High-Resolution Photoelectron Imaging of Cryogenically Cooled BiB_2^- and BiB_3^- Bismuth–Boron Clusters

Published as part of *The Journal of Physical Chemistry A* virtual special issue “Alec Wodtke Festschrift”.

Han-Wen Gao, Hyun Wook Choi, Jie Hui, and Lai-Sheng Wang*



Cite This: *J. Phys. Chem. A* 2024, 128, 3579–3586



Read Online

ACCESS |



Metrics & More

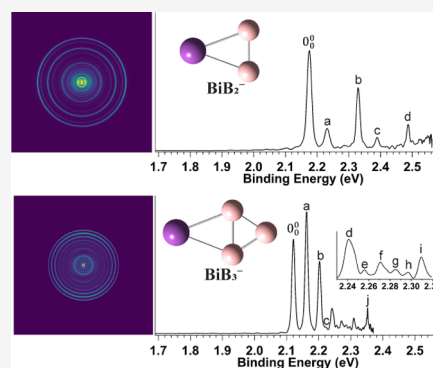


Article Recommendations



Supporting Information

ABSTRACT: We report a high-resolution photoelectron imaging study of cryogenically cooled BiB_2^- and BiB_3^- clusters. Vibrational features are completely resolved for the ground-state detachment transitions, providing critical information about the structures of the anionic clusters and their corresponding neutrals. The electron affinities of BiB_2 and BiB_3 are accurately measured to be 2.174(1) and 2.121(1) eV, respectively. The B–B and Bi–B stretching frequencies are measured to be 1262 and 476 cm^{-1} , respectively, in the ground state of BiB_2 . Three vibrational frequencies are measured for the ground state of BiB_3 : 1194 cm^{-1} (B–B stretching), 782 cm^{-1} (B–B stretching), and 339 cm^{-1} (Bi–B stretching). Both BiB_2^- and BiB_3^- and their neutral ground states are found to have planar C_{2v} structures in which the Bi atom bridges two B atoms. BiB_2^- is found to have a triplet spin state (3B_2), consistent with its complicated photoelectron spectra, whereas BiB_3^- is a doublet (2B_1) and neutral BiB_3 is closed shell (1A_1). Both BiB_2 and BiB_3 consist of peripheral localized Bi–B and B–B σ bonds and delocalized π and σ bonds.



1. INTRODUCTION

Group III–V compounds constitute an important class of semiconductors.¹ Most III–V semiconductors are made of elements in the middle part of the periodic table (aluminum, gallium, and indium with nitrogen, phosphorus, arsenic, and antimony). However, recently, borides of group V elements have drawn significant attention because of the discovery of unusually high thermal conductivity and high ambipolar mobility in boron arsenide.^{2–4} As the heaviest group V element, bismuth was much less studied in group III–V compounds. Bismuth is considered a “green metal” with low toxicity relative to its neighbors,⁵ and it has received increasing interest in materials science and medicinal chemistry.^{6–8} Several theoretical works have predicted that the electronic properties of bismuth boride differ from those of common group III–V compounds^{9–13} and may have the potential for industrial applications.^{14,15} To the best of our knowledge, however, the BiB compound has not yet been synthesized.

Studying bismuth boride clusters in the gas phase affords valuable knowledge about the bonding between bismuth and boron, which may help provide insight into the properties of the bulk material. We have used photoelectron spectroscopy (PES) and theoretical calculations to investigate several Bi–B binary clusters, including BiB_n^- ($n = 4–8$)^{16,17} and dibismuth boride clusters, Bi_2B_n^- ($n = 2–4$).¹⁸ We have also found the Bi–B single bond, the Bi=B double bond, and the $\text{Bi}\equiv\text{B}$ triple bond in BiBO^- , Bi_2B^- , and BiB_2O^- , respectively.^{19,20} In all of the previous studies, anionic clusters were generated by a

laser vaporization supersonic cluster source, which was known to be not highly effective at cooling the vibrational degrees of freedom. Vibrational hot bands make it challenging to obtain vibrationally resolved photoelectron spectra, even under good spectral resolution.^{21,22} Recently, we have demonstrated that the coupling of a cryogenically cooled 3D Paul trap with a laser vaporization cluster source can produce vibrationally cold cluster anions.^{23–25} The cold anion not only allowed us to resolve vibrational features but even the rotational profile for the 0–0 detachment transition of SbO_2^- .²⁵ Combining cryogenically cooled anions and high-resolution photoelectron imaging (PEI), we are able to resolve and assign all of the low-lying electronic states for the BiB diatomic molecule, including all spin–orbit components and their vibrational progressions.²⁶ We have also observed the formation of the closed-shell BiBH^- anion in the ion trap and discovered a $\text{Bi}\equiv\text{B}$ triple bond in the simplest metal boryne complex.²⁷

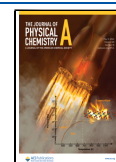
In this paper, we extend our studies using the newly developed cryogenic ion trap coupled with a laser vaporization cluster source to two more complicated Bi/B clusters, BiB_2^-

Received: March 13, 2024

Revised: April 8, 2024

Accepted: April 15, 2024

Published: April 25, 2024



and BiB_3^- . We report high-resolution vibrationally resolved PES data of cryogenically cooled BiB_2^- and BiB_3^- using PEI and compare them with PES data taken from our magnetic-bottle PES apparatus without cryogenic cooling. The BiB_2^- and BiB_3^- clusters have more vibrational modes than the diatomic BiB^- , making them good systems to test the cooling effect of our cryogenic ion trap. The high-resolution PEI data of cold anions provide vibrational fingerprints, which are valuable for the determination of cluster structures. Furthermore, these clusters allow us to adopt a bottom-up approach from BiB^- to BiB_2^- and BiB_3^- to examine how the structures and bonding of Bi–B clusters evolve with the introduction of more boron atoms. We have found that both BiB_2^- and BiB_3^- are planar C_{2v} symmetry, with the Bi atom bridge-bonded to two B atoms. Observations of all totally symmetric modes in the photoelectron spectra of both anions suggest that their neutral ground states have the same C_{2v} symmetry. The bonding between Bi and the B_2 and B_3 units are analyzed, revealing both localized peripheral Bi–B and B–B σ bonds and delocalized π and σ bonds in the planar C_{2v} structures.

2. EXPERIMENTAL AND THEORETICAL METHODS

2.1. Photoelectron Spectroscopy. Two PES techniques were used to investigate the BiB_2^- and BiB_3^- clusters in the current work: a magnetic-bottle PES apparatus with a laser vaporization cluster source and a PEI apparatus newly equipped with a cryogenically cooled ion trap. In general, the magnetic-bottle PES technique allows high photon energies to be used,²⁸ whereas the PEI of cryogenically cooled anions can yield vibrational information.^{21,22}

2.1.1. Magnetic-Bottle Photoelectron Spectroscopy. Details of the magnetic-bottle PES apparatus can be found elsewhere.²⁸ Briefly, the BiB_2^- and BiB_3^- clusters were prepared by laser vaporization of a disk target made with mixed powders of bismuth and ^{10}B -enriched boron. A high-pressure He carrier gas seeded with 5% Ar was used to quench the laser-induced plasma to initiate cluster formation. Clusters formed inside the nozzle were entrained by the carrier gas and cooled by supersonic expansion. After passing through a skimmer, anions in the collimated beam were analyzed by a time-of-flight (TOF) mass spectrometer. The clusters of interest were selected and decelerated before being crossed by a detachment laser. Three photon energies were used in the current study: 532 nm (2.331 eV), 355 nm (3.496 eV), and 266 nm (4.661 eV) from the second, third, and fourth harmonic outputs of a Nd:YAG laser, respectively. Photoelectrons were collected with a >90% efficiency by the magnetic bottle and analyzed in a 3.5 m long electron TOF tube. The electron kinetic energies were calibrated by using the known transitions of the Bi^- atomic anion. The kinetic energy (E_k) resolution ($\Delta E_k/E_k$) of the magnetic-bottle PES analyzer was about 2.5%, that is, ~ 25 meV for electrons with a 1 eV kinetic energy.

2.1.2. Photoelectron Imaging of Cryogenically Cooled Anions. High-resolution PES was conducted on a PEI apparatus newly equipped with a cryogenically cooled 3D Paul trap.^{23–27} The PEI apparatus has been reported in detail previously.²⁹ The laser vaporization cluster source and target were similar to those used on the magnetic-bottle PES apparatus presented above, except that pure He was used as the carrier gas. After passing through a skimmer, the collimated cluster beam traveled directly into a 3D Paul trap cooled to 4.2

K by a two-stage closed-cycle helium refrigerator. Anions in the cluster beam were trapped and collisionally cooled by a mixed He/ H_2 buffer gas (4:1 by volume) for 45 ms before being ejected out of the trap into the extraction region of a TOF mass spectrometer. The clusters of interest were mass-selected and intercepted by a detachment laser in the interaction zone of a velocity map imaging (VMI) system. Photodetachment was performed using a Nd:YAG-pumped dye laser as well as the second and third harmonic outputs from the Nd:YAG laser. Photoelectrons were projected onto a set of micro-channel plates coupled with a phosphor screen and a charge-coupled-device camera. The VMI lens was calibrated using the PE images of Bi^- at various photon energies. The PE images were analyzed by the maximum entropy method (MEVELER).³⁰ The resolution of the VMI system was $\sim 0.6\%$ for electrons with high kinetic energies and as low as 2 cm^{-1} for very slow electrons.

Photoelectron angular distributions (PADs) were obtained from the PE images, which are characterized by the anisotropy parameter (β).³¹ The differential cross section of photoelectrons can be expressed as

$$\frac{d\sigma}{d\Omega} = \left(\frac{\sigma_{\text{tot}}}{4\pi} \right) [1 + \beta P_2(\cos \theta)] \quad (1)$$

where σ_{tot} is the total cross section, P_2 is the second-order Legendre polynomial, and θ is the angle of the photoelectron relative to the laser polarization. Thus, the PADs can be described by

$$I(\theta) \sim [1 + \beta P_2(\cos \theta)] \quad (2)$$

where β has a value ranging from -1 to 2 . This model works well for the single-photon ionization of randomly oriented molecules. According to the electric dipole selection rules, when an electron in an atom with angular momentum l is detached, the outgoing photoelectron wave must carry an angular momentum of $l \pm 1$. For example, if an electron is detached from an s atomic orbital ($l = 0$), the outgoing photoelectron will have $l = 1$ (pure p -wave) with $\beta = 2$. If an electron is detached from an atomic p orbital, the outgoing electron will carry $s + d$ partial waves with $\beta = -1$. It is nontrivial to interpret the β value for electron detachment from molecular orbitals (MOs), which are linear combinations of atomic orbitals. Nevertheless, the β value is still very useful to qualitatively assess the symmetries of the MOs involved in the photodetachment process and provides additional information for spectral assignments.³²

2.2. Theoretical Methods. We carried out theoretical calculations to help interpret the experimental data. Different initial structures of BiB_2^- and BiB_3^- with various spin multiplicities were optimized at the PBE0/aug-cc-pVTZ level of theory.^{33,34} Frequency calculations were carried out to compare with the experimental data and to ensure that the optimized structures were true minima. Vertical excitation energies (VDEs) of neutral species were calculated by using the time-dependent density functional method (TD-DFT) at the PBE0 level of theory. Spin–orbit effects were not treated explicitly in the DFT calculations in the current work, which affected the accuracy of the computed detachment energies for the systems containing the Bi atom. All calculations were performed using the Gaussian 09 program.³⁵ Franck–Condon (FC) factors were computed using the ezFCF program.³⁶ We

employed the adaptive natural density partitioning (AdNDP) method for the chemical bonding analyses.^{37,38}

3. EXPERIMENTAL RESULTS

The photoelectron spectra of BiB_2^- and BiB_3^- measured with the magnetic-bottle apparatus at three photon energies of the Nd:YAG laser are shown in Figures 1 and 2, respectively. The

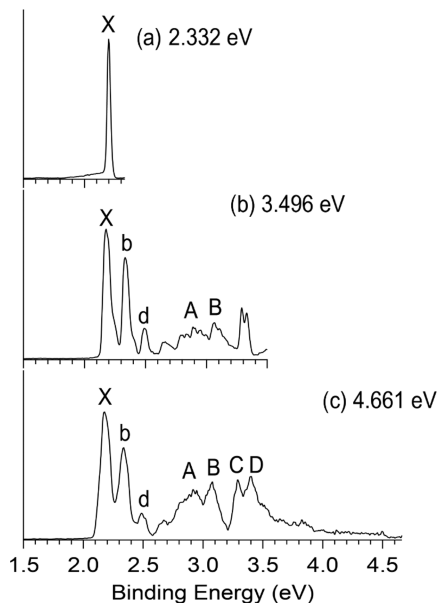


Figure 1. Photoelectron spectra of BiB_2^- at (a) 532 (2.331 eV), (b) 355 (3.496 eV), and (c) 266 nm (4.661 eV) from the magnetic-bottle PES apparatus.

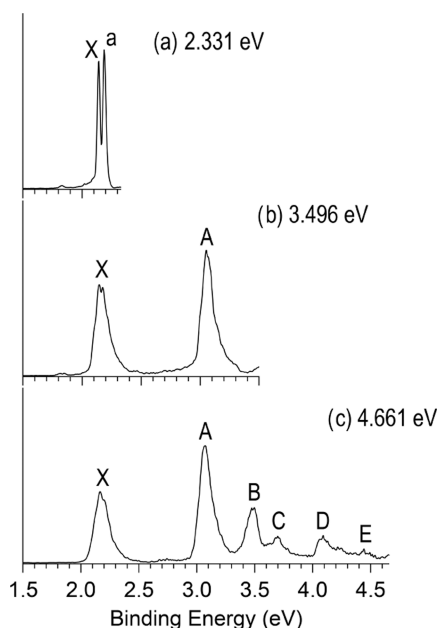


Figure 2. Photoelectron spectra of BiB_3^- at (a) 532 nm (2.331 eV), (b) 355 nm (3.496 eV), and (c) 266 nm (4.661 eV) from the magnetic-bottle PES apparatus.

observed electronic transitions are labeled with capital letters, X, A, B, and ..., whereas the lower-case letters (*b* and *d*) in Figure 1 denote vibrational features. Band X represents the transition from the ground state of the anion to that of the

neutral, and bands A, B, ..., indicate transitions to excited electronic states of the neutral. High-resolution PE images and spectra of cryogenically cooled BiB_2^- are shown in Figure 3

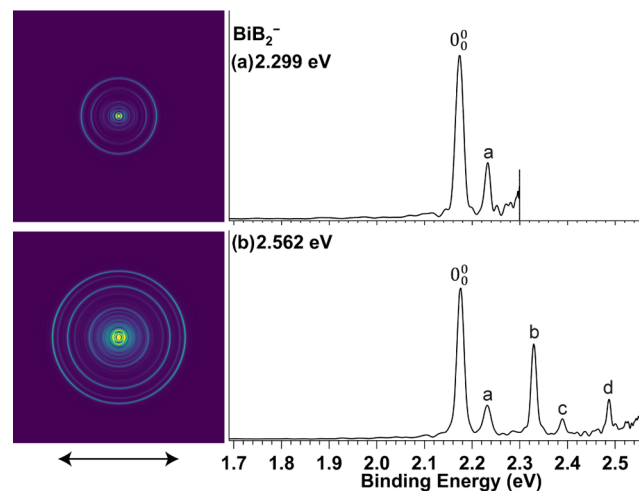


Figure 3. Photoelectron images and spectra of cryogenically cooled BiB_2^- at (a) 539.30 nm (2.299 eV) and (b) 483.94 nm (2.562 eV). The double arrow below the image indicates laser polarization.

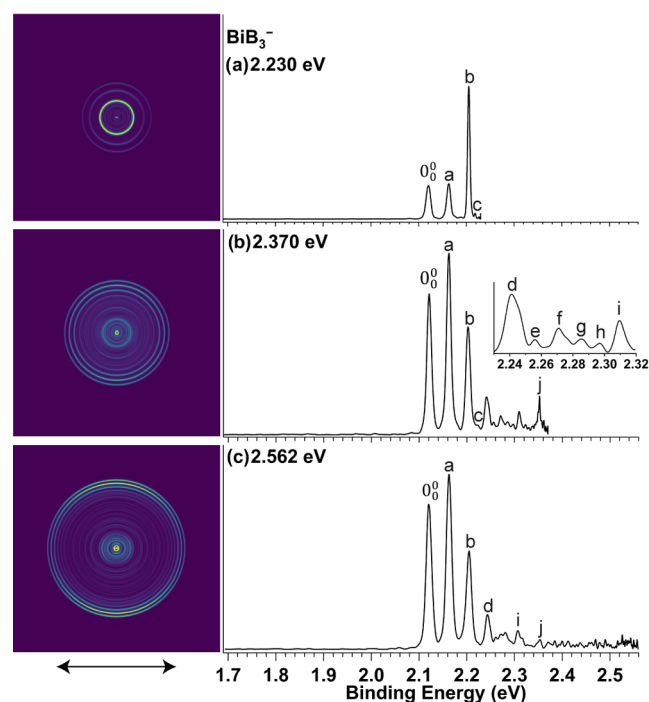


Figure 4. Photoelectron images and spectra of cryogenically cooled BiB_3^- at (a) 555.98 nm (2.230 eV), (b) 523.14 nm (2.370 eV), and (c) 483.94 nm (2.562 eV). The double arrow below the image indicates the laser polarization.

and those for BiB_3^- are shown in Figure 4 for their respective ground-state detachment transitions. Rich vibrational structures are resolved in the high-resolution PEI data for the ground-state transition in each case, providing valuable information for elucidating the structures and bonding of the underlying clusters.

3.1. Photoelectron Spectra of BiB_2^- . The data taken with the magnetic-bottle apparatus resolved a vibrational progression for the ground-state transition (defined by peaks *b* and *d*), with a large vibrational spacing of $\sim 1300 \text{ cm}^{-1}$ and congested vibronic features for the higher binding energy detachment transitions (Figure 1). Four bands can be tentatively identified, and the VDEs of these detachment transitions are given in Table S1. The PEI data (Figure 3) resolve more weak vibrational features (*a*, *c*), in addition to the vibrational progression represented by *b* and *d* in band X. The high-resolution PEI spectrum at 2.299 eV (Figure 3a) yields an accurate electron affinity (EA) of 2.174 eV for BiB_2^- and a 476 cm^{-1} frequency for the weak low-frequency mode defined by peak *a*. The high-resolution PEI spectrum at 2.562 eV (Figure 3b) yields an accurate frequency of 1262 cm^{-1} for the high-frequency mode. Peak *c* is a combinational vibrational level between the high- and low-frequency modes. All of the vibrational peaks have *p*-type angular distributions with positive β values. The binding energies of the vibrational peaks, their β values, and assignments are given in Table 1.

Table 1. Measured Binding Energies (BEs) and Assignments of the Ground-State Detachment Transition of BiB_2^- from the PEI Data^c

peak	assignment	BE (eV) ^a	frequency (cm^{-1}) ^a	β
0_0^0	0_0^0	2.174(1)		0.3
<i>a</i>	1_0^1	2.233(1)	476(8)	0.3
<i>b</i>	3_0^1	2.330(2)	1262(12) ^b	0.5
<i>c</i>	$3_0^1 1_0^1$	2.390(2)		0.3
<i>d</i>	3_0^2	2.487(1)		0.2

^aFor the ^{10}B isotope, the numbers in parentheses represent the uncertainty in the last digit. ^bAverage of the two vibrational quanta. ^cThe vibrational frequencies of each peak and their β values are also given.

3.2. Photoelectron Spectra of BiB_3^- . The PE spectra of BiB_3^- taken with the magnetic-bottle apparatus (Figure 2) reveal six well-resolved detachment transitions (X, A–E). The 2.331 eV spectrum cuts off band X, resolving two vibrational peaks (Figure 2a). The VDEs for all of the detachment transitions are given in Table S2. A very weak signal was observed in the spectra at 2.331 eV (Figure 2a) and 3.496 eV (Figure 2b) but not at 4.661 eV (Figure 2c). It was probably due to a minute contaminant. High-resolution PEI data of cryogenically cooled BiB_3^- were taken at 2.230, 2.370, and 2.562 eV to better resolve the vibrational features for the ground-state detachment transition, as shown in Figure 4. A broad vibrational progression is resolved. The 0–0 transition defines an accurate EA of 2.121 eV for BiB_3^- . The main vibrational progression (peaks *a*, *b*, *d*, and *g*) is well resolved with a frequency of 339 cm^{-1} . A very weak vibrational feature (peak *c*) is discernible with a frequency of 782 cm^{-1} in Figure 4a,b. Peaks *e* and *h* should be the combinational vibrational levels between the mode represented by peak *c* and the main vibrational progression. Similarly, a third mode and its combinations with the main vibrational progression are assigned to peaks *f*, *i*, and *j* with a frequency of 1194 cm^{-1} . All of the vibrational peaks have *s* + *d* type angular distribution with negative β values. The binding energies of the observed vibrational features and their β values are listed in Table 2. It should be noted that there is a significant threshold enhancement for peak *b* in Figure 4a and peak *j* in Figure

Table 2. Measured Binding Energies (BEs) and Assignments of the Ground-State Detachment Transition of BiB_3^- from the PEI Data^{b,d}

peak	assignment	BE (eV) ^a	frequency (cm^{-1}) ^a	β
0_0^0	0_0^0	2.121(1)		−0.6
<i>a</i>	2_0^1	2.163(1)	339(8)	−0.4
<i>b</i>	2_0^2	2.205(1)		−0.4
<i>c</i>	4_0^1	2.218(1)	782(16)	−0.2
<i>d</i>	2_0^3	2.242(2)		−0.3
<i>e</i>	$2_0^1 4_0^1$	2.256(2)		
<i>f</i>	6_0^1	2.271(2)	1194(20) ^c	−0.3
<i>g</i>	2_0^4	2.286(5)		−0.2
<i>h</i>	$2_0^2 4_0^1$	2.297(2)		
<i>i</i>	$2_0^1 6_0^1$	2.310(2)		−0.6
<i>j</i>	$2_0^2 6_0^1$	2.352(1)		−0.3

^aFor the ^{10}B isotope. The numbers in parentheses represent the uncertainty in the last digit. ^bThese β values are obtained from the PE image taken at 2.370 eV. ^cAverage from peaks *f*, *i*, and *j*. ^dThe vibrational frequency of each peak and the β value are also given.

4b. The angular distribution of peak *b* is also more isotropic in Figure 4a, suggesting that the *s* partial wave is more dominating near threshold, consistent with its enhanced intensity according to the Wigner threshold law.³⁹

4. THEORETICAL RESULTS

4.1. BiB_2^- . The observed vibrational information was utilized to guide our theoretical search for the structure of BiB_2^- . There is a vibration mode exhibiting a high frequency of 1266 cm^{-1} , which should originate from the B–B stretching,⁴⁰ suggesting that BiB_2^- must contain an intact B_2 unit. Using this insight, we computed two structures for BiB_2^- (Figure 5a) and

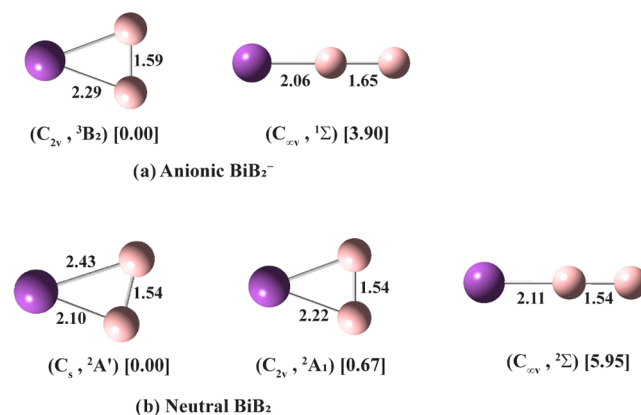


Figure 5. Structures and relative energies of different isomers for (a) BiB_2^- and (b) BiB_2 . The relative energies (kcal mol^{-1}) calculated at the PBE0/aug-cc-pVTZ level are given in square brackets. The point group symmetries and electronic states are also given. The bond lengths are given in Å.

found that the C_{2v} structure with the Bi atom bridging the B_2 unit is lower in energy. The linear Bi–B–B isomer is higher in energy by 3.90 kcal/mol at the PBE0 level. The C_{2v} ground state was found to have a triplet spin state with a valence electron configuration of $\{ \dots (4b_2)^2 (3b_1)^2 (8a_1)^2 (9a_1)^1 (5b_2)^1 \}$ (3B_2), whereas the linear isomer was found to be closed shell with a valence electron configuration of $\{ \dots (8\sigma)^2 (5\pi)^2 (6\pi)^2 (9\sigma)^2 \}$ ($^1\Sigma^+$).

By removal of an electron from the C_{2v} BiB_2^- , DFT calculations yielded a C_s neutral ground state with the Bi atom displaced away from the C_{2v} axis (Figure 5b). However, if the symmetry is constrained to C_{2v} the structure was found to have an imaginary frequency along the antisymmetric stretching mode, but it is only 0.67 kcal/mol higher in energy at PBE0. By removal of an electron from the linear BiB_2^- , DFT calculations still yielded a linear neutral BiB_2 state, which is 5.95 kcal/mol higher in energy, as shown in Figure 5b.

4.2. BiB_3^- . The low-lying structures of BiB_3^- indicate that Bi does not disrupt the B–B bond. Thus, we tested initial structures for BiB_3^- with the Bi atom bonded to different positions around the B_3 triangle.⁴¹ We were able to find only one stable planar structure with Bi bonded to one side of the B_3 triangle (C_{2v} , $^2\text{B}_1$), as shown in Figure 6a. A similar C_{2v} ,

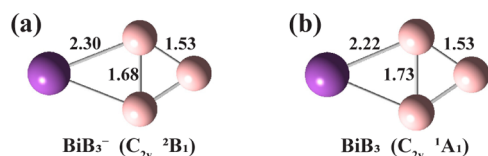


Figure 6. Global minimum of BiB_3^- (a) and its corresponding neutral (b). The point group symmetry and electronic states are also given. The bond lengths are given in Å.

structure with a quartet spin state and another isomer with Bi bonded to an apex atom of the B_3 triangle are found to be much higher in energy (Figure S1). The global minimum of BiB_3^- has a valence electron configuration of $\{... (3b_1)^2(5b_2)^2(10a_1)^2(4b_1)^1\}$ ($^2\text{B}_1$). Detaching an electron from the $4b_1$ SOMO yields a C_{2v} closed-shell neutral ground state ($^1\text{A}_1$) for BiB_3 , as shown in Figure 6b.

5. DISCUSSION

5.1. Comparison of the Experimental Results with the Theoretical Calculations. The observed vibrational structures for the ground-state detachment transitions from the PEI experiments of cold BiB_2^- and BiB_3^- are critical in determining their structures.

5.1.1. BiB_2^- and BiB_2 . Since the triangular and linear structures of BiB_2^- (Figure 5a) are close in energy at the PBE0 level, our first objective is to ascertain which isomer is indeed the global minimum. Molecular vibrations provide critical fingerprints for molecular structures. We calculated the vibrational frequencies and Franck–Condon (FC) factors for both isomers, as shown in Figure 7. The FC calculations were done by using the ezFCF program³⁶ with the computed anion and neutral structures, as well as their calculated frequencies.

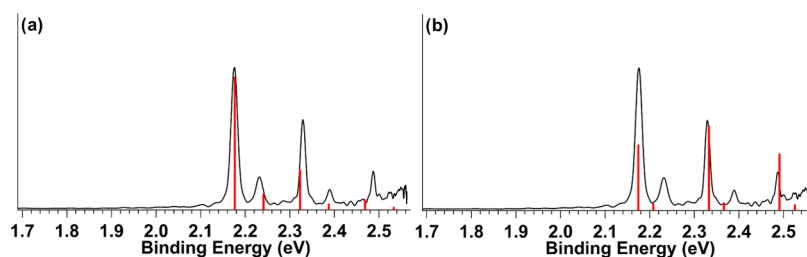


Figure 7. Comparison of the PE spectrum of BiB_2^- at 2.562 eV with the calculated FC factors (red) for (a) the C_{2v} isomer and (b) the linear isomer.

The computed FC factors for the linear isomer (Figure 7b) clearly do not agree with those of the experiment. Both the FC factors for the main progression and the frequency for the weak low-frequency bending mode are not consistent with the experiment. For the triangular structure, the corresponding neutral has two possibilities: either C_s or C_{2v} . Even though the DFT calculation gave a C_s ground state, this structure can be readily ruled out because a C_s final neutral state would suggest a highly active Bi–B antisymmetric stretching mode with a calculated frequency of 252 cm^{-1} , which was not observed in the experiment. For the C_{2v} neutral ground state, Figure 7a shows that the computed FC factors are in good agreement with the experimental observation. The two observed modes represent the two totally symmetric vibrational modes of C_{2v} BiB_2 : the symmetric B–B stretching mode (ν_3) and the symmetric Bi–B stretching mode (ν_1), as shown in Figure 8a.

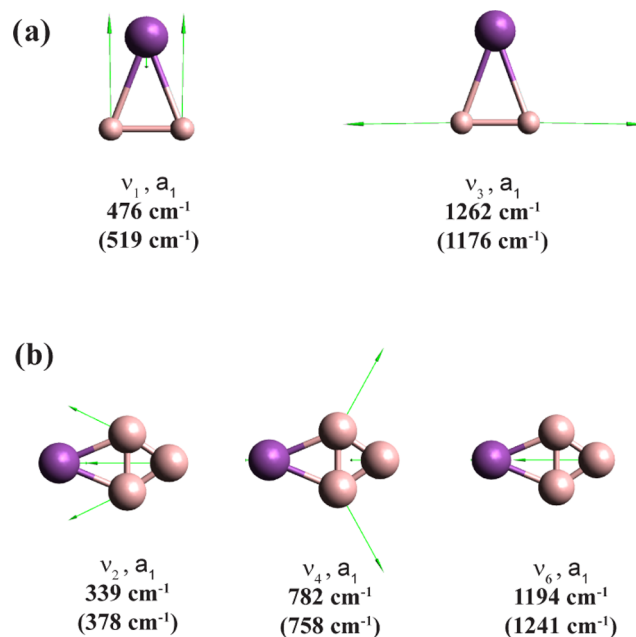


Figure 8. Displacement vectors and observed frequencies for total symmetric vibrational modes of (a) BiB_2 and (b) BiB_3 . The calculated frequencies are given in parentheses.

The measured frequencies for the ν_3 mode (1262 cm^{-1}) and the ν_1 mode (476 cm^{-1}) agree well with the computed frequencies of 1176 and 519 cm^{-1} , respectively. The antisymmetric mode that is not observed experimentally has an imaginary frequency in the PBE0 calculation, as shown in Figure S2a, whereas the computed frequency for the antisymmetric mode of C_s BiB_2 is 252 cm^{-1} . It should be

noted that the C_{2v} structure is only 0.67 kcal/mol higher in energy at the PBE0 level than the C_s structure (Figure 5b). Thus, the potential energy surface along the antisymmetric ν_2 coordinate seems to be fairly flat and the zero point level might be above the saddle point at the C_{2v} symmetry. In other words, the vibrationally averaged structure of BiB_2 may have a C_{2v} symmetry. It is also possible that the C_{2v} saddle point is a computational artifact because there is no experimental evidence for the C_s distortion in the neutral final state. Clearly, more accurate calculations by including spin–orbit couplings and electron correlation effects are needed to treat BiB_2 properly.

We have performed TD-DFT calculations of the C_{2v} BiB_2^- to understand the higher detachment transitions from the magnetic-bottle apparatus (Figure 1). The higher spectral features are surprisingly complicated, consistent with the open-shell nature of the C_{2v} BiB_2^- anion, which can lead to both doublet and quartet final states via one-electron detachment processes. All of the valence MOs of BiB_2^- are shown in Figure S3. The calculated VDEs for all detachment channels are summarized and compared with the experimental data in Table S1. As mentioned above, there are clear challenges in using the DFT method to treat the open-shell BiB_2 . Thus, the TD-DFT results for the excited-state calculations are not very accurate, and they are used tentatively to assign the higher detachment channels, as shown in Table S1.

5.1.2. BiB_3^- and BiB_3 . The valence MOs for the C_{2v} global minimum of BiB_3^- are displayed in Figure S4. Its SOMO is an antibonding π orbital between the Bi $6p_z$ orbital and the π orbital on the B_3 motif. The $s + d$ type angular distribution observed in the PEI data is consistent with the nature of the SOMO. Thus, it is expected that detaching the electron from the SOMO should result in shorter Bi–B bonds in neutral BiB_3 , in perfect accord with the optimized structures (Figure 6b). Since the C_{2v} symmetry is maintained from BiB_3^- to BiB_3 , only totally symmetric modes are FC-active. We have indeed identified all three totally symmetric modes: ν_2 , ν_4 , and ν_6 (Figures 8b and S2b). As shown in Table 2, the vibrational peaks *a*, *b*, *d*, and *g* correspond to mode ν_2 . Peak *c* corresponds to mode ν_4 , and peaks *e* and *h* are the combinational modes between ν_4 and ν_2 . Peak *f* corresponds to mode ν_6 , and peaks *i* and *j* are the combinational modes between ν_6 and ν_2 . The three totally symmetric modes and their computed frequencies are given in Figure 8b and compared to the measured frequencies. We also computed the FC factors, which are in good agreement with the experiment, as shown in Figure S5. The good agreement between the calculated frequencies and the experimental observation unequivocally confirms the C_{2v} global minimum structure of BiB_3^- and its corresponding neutral. All six normal modes for BiB_3 and their computed frequencies are given in Figure S2b.

The closed-shell nature of BiB_3 makes it much more straightforward to conduct TD-DFT calculations to explain the higher detachment channels of BiB_3^- , as shown in Table S2. Overall, the computed VDEs are in good agreement with the experimental data.

5.2. Chemical Bonding Analyses. The strong relativistic effects in Bi stabilize the $6s$ electrons,⁴² which are relatively inert and do not participate in chemical bonding. The lack of s – p hybridization and the large size differences imply a relatively weak Bi–B bond, so that the Bi atom does not disrupt the B–B bonds in BiB_x^- clusters, as also shown previously in large clusters for $x = 4$ – 8 .^{17,18} Thus, even though

BiB_2^- and BiB_3^- are isovalent with B_2N^- and B_3N^- , their structures and bonding are completely different. The global minima of both B_2N^- and B_3N^- and their neutral counterparts have been reported to be linear B–N–B and B–N–B–B species, respectively, due to the strong B–N bonds.^{43,44}

We analyzed the chemical bonding in BiB_2 and BiB_3 using AdNDP,^{37,38} as shown in Figures 9 and 10, respectively. We

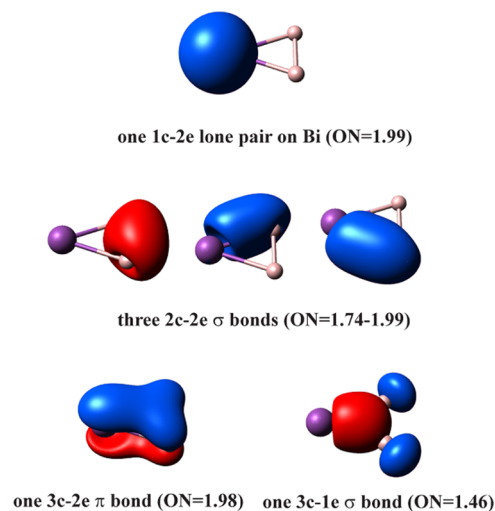


Figure 9. AdNDP bonding analysis for BiB_2 . ON stands for occupation number.

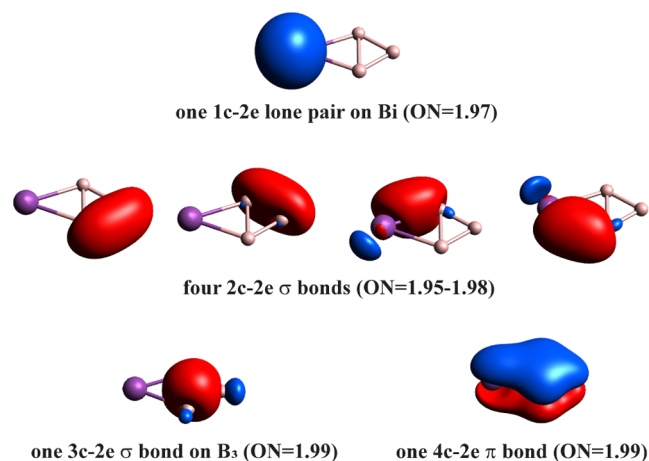


Figure 10. AdNDP bonding analysis for BiB_3 . ON stands for the occupation number.

found the expected $1c$ – $2e$ $6s^2$ lone pair on Bi and three $2c$ – $2e$ σ bonds around the BiB_2 triangle. In addition, we also found one $3c$ – $2e$ delocalized π bond and one delocalized $3c$ – $1e$ σ bond. The large occupation number ($\text{ON} = 1.46$) for the $3c$ – $1e$ bond indicates contributions to the delocalized bonds from the Bi–B $2c$ – $2c$ bonds, which have an ON of only 1.74.

The lack of s – p hybridization in Bi suggests that it can only use its three $6p$ orbitals to bond with B_2 . The $6p_z$ orbital forms the delocalized π bond with B_2 . However, the $6p_x$ and $6p_y$ orbitals are not optimal to form σ bonds with B_2 , which is probably responsible for the low ON value for the Bi–B σ bonds and may also explain why the C_{2v} structure in neutral BiB_2 is a saddle point at the PBE0 level. It should be noted that the B–B bond in BiB_2 , judged by the B–B bond length (1.54 Å) and B–B stretching frequency (1266 cm^{-1}), is significantly

strengthened, relative to the bare B₂ dimer (1.578 Å, 1053 cm⁻¹).⁴⁰ This observation is consistent with other transition-metal and lanthanide MB₂ species, in which the B–B bond is similarly strengthened due to back-donation from the metal to the bonding π orbital of B₂.^{45–47} Both the delocalized π and σ bonds strengthen the B–B bond.

The bonding in closed-shell BiB₃ is similar to that in BiB₂. The AdNDP analysis reveals the expected 1c–2e lone pair on Bi, four 2c–2e bonds around the periphery of BiB₃, one delocalized 3c–2e σ bond on the B₃ motif, and one delocalized 4c–2e π bond. This leaves no direct B–B bond between the two B atoms bridged by the Bi atom other than the delocalized bonds. It can be seen that the B–B bond is broken to form the Bi–B bonds. Several planar transition-metal MB₃ clusters with C_{2v} symmetry have been reported before;^{48–50} strong M–B bonds have been shown to weaken the B–B bond that coordinates to the metal atom. In TaB₃, the very strong Ta–B bonds result in a fan-shaped structure,⁴⁸ whereas the weaker M–B bonds in MnB₃ and IrB₃ lead to relatively short B–B distances between the two bridged B atoms. The Bi–B bond length is 2.22 Å in BiB₃, which is shorter than the single Bi–B covalent bond according to Pyykko's single-bond covalent radii (2.36 Å),⁵¹ consistent with the AdNDP bonding analysis.

6. CONCLUSIONS

In conclusion, we report a high-resolution photoelectron imaging study of two Bi-doped boron clusters, BiB₂⁻ and BiB₃⁻, which were produced by a laser vaporization cluster source and cooled in a cryogenic Paul trap. The vibrationally resolved photoelectron spectra are shown to serve as valuable molecular fingerprints for structural determination. The global minima of both BiB₂⁻ and BiB₃⁻ and their neutrals are found to have planar C_{2v} structures, with the Bi atom bridging two B atoms. All of the totally symmetric vibrational modes are resolved for the ground-state transitions in both systems. The Bi atoms engage in σ bonding with the B atoms, and the out-of-plane 6p_z orbital of Bi can participate in delocalized π bonding with B₂ or B₃.

■ ASSOCIATED CONTENT

SI Supporting Information

The Supporting Information is available free of charge at <https://pubs.acs.org/doi/10.1021/acs.jpca.4c01672>.

The low-lying isomer of BiB₃⁻, normal modes of vibration for BiB₂ and BiB₃, valence molecular orbitals of BiB₂⁻ and BiB₃⁻, FC calculations for the ground detachment transition of BiB₃⁻, and the measured vertical electron detachment energies of BiB₂⁻ and BiB₃⁻ and their comparison with TD-DFT calculations (PDF)

■ AUTHOR INFORMATION

Corresponding Author

Lai-Sheng Wang – Department of Chemistry, Brown University, Providence, Rhode Island 02912, United States; orcid.org/0000-0003-1816-5738; Email: Lai-Sheng_Wang@brown.edu

Authors

Han-Wen Gao – Department of Chemistry, Brown University, Providence, Rhode Island 02912, United States

Hyun Wook Choi – Department of Chemistry, Brown University, Providence, Rhode Island 02912, United States
Jie Hui – Department of Chemistry, Brown University, Providence, Rhode Island 02912, United States

Complete contact information is available at: <https://pubs.acs.org/10.1021/acs.jpca.4c01672>

Notes

The authors declare no competing financial interest.

■ ACKNOWLEDGMENTS

This work was supported by the National Science Foundation (Grant No. CHE-2403841). The calculation was performed using computational resources and services provided by CCV of Brown University.

■ REFERENCES

- (1) Vurgaftman, I.; Meyer, J. R.; Ram-Mohan, L. R. Band parameters for III-V compound semiconductors and their alloys. *J. Appl. Phys.* **2001**, *89*, 5815–5875.
- (2) Lindsay, L.; Broido, D. A.; Reinecke, T. L. First-principles determination of ultrahigh thermal conductivity of boron arsenide: A competitor for diamond? *Phys. Rev. Lett.* **2013**, *111*, No. 025901, DOI: [10.1103/PhysRevLett.111.025901](https://doi.org/10.1103/PhysRevLett.111.025901).
- (3) Kang, J. S.; Li, M.; Wu, H.; Nguyen, H.; Hu, Y. Experimental observation of high thermal conductivity in boron arsenide. *Science* **2018**, *361*, 575–578.
- (4) Shin, J.; Gamage, G. A.; Ding, Z.; Chen, K.; Tian, F.; Qian, X.; Zhou, J.; Lee, H.; Zhou, J.; Shi, L.; et al. High ambipolar mobility in cubic boron arsenide. *Science* **2022**, *377*, 437–440.
- (5) Mohan, R. Green bismuth. *Nat. Chem.* **2010**, *2*, 336.
- (6) Ramler, J.; Lichtenberg, C. Bismuth species in the coordination sphere of transition metals: synthesis, bonding, coordination chemistry, and reactivity of molecular complexes. *Dalton Trans.* **2021**, *50*, 7120–7138.
- (7) Zhang, Y.; Liu, Y.; Xu, Z.; Ye, H.; Yang, Z.; You, J.; Liu, M.; He, Y.; Kanatzidis, M. G.; Liu, S. Nucleation-controlled growth of superior lead-free perovskite Cs₃Bi₂I₉ single-crystals for high-performance X-ray detection. *Nat. Commun.* **2020**, *11*, No. 2304, DOI: [10.1038/s41467-020-16034-w](https://doi.org/10.1038/s41467-020-16034-w).
- (8) Salvador, J. A. R.; Figueiredo, S. A. C.; Pinto, R. M. A.; Silvestre, S. M. Bismuth compounds in medicinal chemistry. *Future Med. Chem.* **2012**, *4*, 1495–1523.
- (9) Madouri, D.; Ferhat, M. How do electronic properties of conventional III–V semiconductors hold for the III–V boron bismuth BBi compound? *Phys. Status Solidi B* **2005**, *242*, 2856–2863.
- (10) Cui, S.; Feng, W.; Hu, H.; Feng, Z.; Wang, Y. First principles studies of phase stability, electronic and elastic properties in BBi compound. *Comput. Mater. Sci.* **2010**, *47*, 968–972.
- (11) Ferhat, M.; Zaoui, A. Structural and electronic properties of III–V bismuth compounds. *Phys. Rev. B* **2006**, *73*, No. 115107, DOI: [10.1103/PhysRevB.73.115107](https://doi.org/10.1103/PhysRevB.73.115107).
- (12) Shahri, R. P.; Akhtar, A. First principles study and comparison of vibrational and thermodynamic properties of XBi (X = In, Ga, B, Al). *Chin. Phys. B* **2017**, *26*, No. 093107.
- (13) Yalcin, B. G.; Bagci, S.; Ustundag, M.; Aslan, M. Electronic and optical properties of BBi and AlBi. *Comput. Mater. Sci.* **2015**, *98*, 136–141.
- (14) Bagci, S.; Yalcin, B. G. Structural, mechanical, electronic and optical properties of BBi, BP and their ternary alloys BBi_{1-x}P_x. *J. Phys. D: Appl. Phys.* **2015**, *48*, No. 475304.
- (15) Fan, J.; Hao, W.; Fu, C.; Chen, Z.; Liang, R.; Lian, C.; Zhang, Q.; Li, G. Construction of efficient bismuth/boron-based flexible electrodes in organic media toward neutral hydrogen evolution. *J. Mater. Chem. A* **2022**, *10*, 1535–1546.
- (16) Chen, W. J.; Kulichenko, M.; Choi, H. W.; Cavanagh, J.; Yuan, D. F.; Boldyrev, A. I.; Wang, L. S. Photoelectron spectroscopy of size-

selected bismuth-boron clusters: BiB_n^- ($n = 6-8$). *J. Phys. Chem. A* **2021**, *125*, 6751–6760.

(17) Choi, H. W.; Chen, W. J.; Kocheril, G. S.; Yuan, D. F.; Wang, L. S. The structures and bonding of bismuth-doped boron clusters: BiB_4^- and BiB_5^- . *Inorganics* **2023**, *11*, 405.

(18) Cheung, L. F.; Czekner, J.; Kocheril, G. S.; Wang, L. S. High resolution photoelectron imaging of boron-bismuth binary clusters: Bi_2B_n^- ($n = 2-4$). *J. Chem. Phys.* **2019**, *150*, No. 064304, DOI: 10.1063/1.5084170.

(19) Jian, T.; Cheung, L. F.; Chen, T. T.; Wang, L. S. Bismuth-boron multiple bonding in BiB_2O^- and Bi_2B^- . *Angew. Chem., Int. Ed.* **2017**, *56*, 9551–9555.

(20) Jian, T.; Lopez, G. V.; Wang, L. S. Photoelectron spectroscopy of BiAu^- and BiBO^- : Further evidence of the analogy between Au and boronyl. *J. Phys. Chem. B* **2016**, *120*, 1635–1640.

(21) Wang, L. S. Electrospray photoelectron spectroscopy: From multiply-charged anions to ultracold anions. *J. Chem. Phys.* **2015**, *143*, No. 040901, DOI: 10.1063/1.4927086.

(22) Weichman, M. L.; Neumark, D. M. Slow photoelectron velocity-map imaging of cryogenically cooled anions. *Annu. Rev. Phys. Chem.* **2018**, *69*, 101–124.

(23) Kocheril, G. S.; Gao, H. W.; Yuan, D. F.; Wang, L. S. Photoelectron imaging of cryogenically cooled BiO^- and BiO_2^- anions. *J. Chem. Phys.* **2022**, *157*, No. 171101, DOI: 10.1063/5.0127877.

(24) Kocheril, G. S.; Gao, H. W.; Wang, L. S. Observation of a long-lived triplet excited state and strong electron correlation effects in the copper oxide anion (CuO^-) using cryogenic photoelectron imaging. *J. Chem. Phys.* **2023**, *158*, No. 236101, DOI: 10.1063/5.0151516.

(25) Kocheril, G. S.; Gao, H. W.; Wang, L. S. Vibrationally- and rotationally-resolved photoelectron imaging of cryogenically-cooled SbO_2^- . *Mol. Phys.* **2024**, *122*, No. e2182610, DOI: 10.1080/00268976.2023.2182610.

(26) Gao, H. W.; Choi, H. W.; Hui, J.; Chen, W. J.; Kocheril, G. S.; Wang, L. S. On the electronic structure and spin-orbit coupling of BiB from photoelectron imaging of cryogenically-cooled BiB^- anion. *J. Chem. Phys.* **2023**, *159*, No. 114301, DOI: 10.1063/5.0170325.

(27) Gao, H. W.; Hui, J.; Wang, L. S. Observation of an electron-precise metal borane complex: $[\text{Bi}\equiv\text{BH}]^-$. *Chem. Commun.* **2023**, *59*, 12431–12434.

(28) Wang, L. S. Photoelectron spectroscopy of size-selected boron clusters: from planar structures to borophenes and borospherenes. *Int. Rev. Phys. Chem.* **2016**, *35*, 69–142.

(29) León, I.; Yang, Z.; Liu, H. T.; Wang, L. S. The design and construction of a high-resolution velocity-map imaging apparatus for photoelectron spectroscopy studies of size-selected clusters. *Rev. Sci. Instrum.* **2014**, *85*, No. 083106, DOI: 10.1063/1.4891701.

(30) Dick, B. MELEXIR: Maximum entropy Legendre expanded image reconstruction. A fast and efficient method for the analysis of velocity map imaging or photoelectron imaging data. *Phys. Chem. Chem. Phys.* **2019**, *21*, 19499–19512.

(31) Cooper, J.; Zare, R. N. Angular distribution of photoelectrons. *J. Chem. Phys.* **1968**, *48*, 942–943.

(32) Sanov, A.; Mabbs, R. Photoelectron imaging of negative ions. *Int. Rev. Phys. Chem.* **2008**, *27*, 53–85.

(33) Adamo, C.; Barone, V. Toward reliable density functional methods without adjustable parameters: The PBE0 model. *J. Chem. Phys.* **1999**, *110*, 6158–6170.

(34) Dunning, T. H. Gaussian basis sets for use in correlated molecular calculations. I. The atoms boron through neon and hydrogen. *J. Chem. Phys.* **1989**, *90*, 1007–1023.

(35) Frisch, M. J.; Trucks, G. W.; Schlegel, H. B.; Scuseria, G. E.; Robb, M. A.; Cheeseman, J. R.; Scalmani, G.; Barone, V.; Petersson, G. A.; Nakatsuji, H. et al. *Gaussian 09*, Revision A.1; Gaussian, Inc.: Wallingford, CT, 2009.

(36) Gozem, S.; Krylov, A. I. The ezSpectra suite: an easy-to-use toolkit for spectroscopy modeling. *WIREs Comp. Mol. Sci.* **2021**, *12*, No. e1546, DOI: 10.1002/wcms.1546.

(37) Zubarev, D. Y.; Boldyrev, A. I. Developing paradigms of chemical bonding: adaptive natural density partitioning. *Phys. Chem. Chem. Phys.* **2008**, *10*, 5207–5217.

(38) Zubarev, D. Y.; Boldyrev, A. I. Revealing intuitively assessable chemical bonding patterns in organic aromatic molecules via adaptive natural density partitioning. *J. Org. Chem.* **2008**, *73*, 9251–9258.

(39) Wigner, E. P. On the behavior of cross sections near threshold. *Phys. Rev.* **1948**, *73*, 1002–1009.

(40) The vibrational frequency of the $^{11}\text{B}_2$ dimer is known to be 1052.74 cm^{-1} Bredohl, H.; Dubois, I.; Nzohabonayo, P. The emission spectrum of B_2 . *J. Mol. Spectrosc.* **1982**, *93*, 281–285.

(41) Zhai, H. J.; Wang, L. S.; Alexandrova, A. N.; Boldyrev, A. I.; Zakrzewski, V. G. A photoelectron spectroscopy and *ab initio* study of B_3^- and B_4^- anions and their neutrals. *J. Phys. Chem. A* **2003**, *107*, 9319–9328.

(42) Pyykkö, P. Relativistic effects in structural chemistry. *Chem. Rev.* **1988**, *88*, 563–594.

(43) Asmis, K. R.; Taylor, T. R.; Neumark, D. M. Anion photoelectron spectroscopy of B_2N^- . *J. Chem. Phys.* **1999**, *111*, 8838–8851.

(44) Asmis, K. R.; Taylor, T. R.; Neumark, D. M. Anion photoelectron spectroscopy of B_3N^- . *J. Chem. Phys.* **1999**, *111*, 10491–10500.

(45) Merriles, D. M.; Tomchak, K. H.; Nielson, C.; Morse, M. D. Early transition metals strengthen the B_2 bond in MB_2 complexes. *J. Am. Chem. Soc.* **2022**, *144*, 7557–7561.

(46) Robinson, P. J.; Liu, G.; Ciborowski, S.; Martinez-Martinez, C.; Chamorro, J. R.; Zhang, X.; McQueen, T. M.; Bowen, K. H.; Alexandrova, A. N. Mystery of three borides: differential metal-boron bonding governing superhard structures. *Chem. Mater.* **2017**, *29*, 9892–9896.

(47) Wang, Z. L.; Chen, T. T.; Chen, W. J.; Li, W. L.; Zhao, J.; Jiang, X. L.; Li, J.; Wang, L. S.; Hu, H. S. The smallest 4f-metal-aromatic molecule of cyclo- PrB_2^- with Pr–B multiple bonds. *Chem. Sci.* **2022**, *13*, 10082–10094.

(48) Li, W. L.; Ivanov, A. S.; Federič, J.; Romanescu, C.; Černušák, I.; Boldyrev, A. I.; Wang, L. S. On the way to the highest coordination number in the planar metal-centered aromatic Ta@B_{10}^- cluster: evolution of the structures of TaB_n^- ($n = 3-8$). *J. Chem. Phys.* **2013**, *139*, No. 104312, DOI: 10.1063/1.4820401.

(49) Czekner, J.; Cheng, L. F.; Kocheril, G. S.; Kulichenko, M.; Boldyrev, A. I.; Wang, L. S. High-resolution photoelectron imaging of IrB_3^- : observation of a π -aromatic B_3^+ ring coordinated to a transition metal. *Angew. Chem., Int. Ed.* **2019**, *58*, 8877–8881, DOI: 10.1002/anie.201902406.

(50) Cheung, L. F.; Czekner, J.; Kocheril, G. S.; Wang, L. S. High-resolution photoelectron imaging of MnB_3^- : probing the bonding between the aromatic B_3 cluster and 3d transition metals. *J. Chem. Phys.* **2020**, *152*, No. 244306, DOI: 10.1063/5.0013355.

(51) Pyykkö, P. Additive covalent radii for single-, double-, and triple-bonded molecules and tetrahedrally bonded crystals: a summary. *J. Phys. Chem. A* **2015**, *119*, 2326–2337.